



Promoting electrocatalytic hydrogenation of 5-hydroxymethylfurfural using buffer electrolytes as proton-donating motifs: Theoretical predictions and experimental validations

Xiao-Qiang Pan¹, Xin-Yu Zhang¹, Gui-Xiang Huang, Shu-Chuan Mei, Jia-Wei Huang, Jie-Jie Chen, Wu-Jun Liu^{*}, Han-Qing Yu^{*}

CAS Key Laboratory of Urban Pollutant Conversion, Department of Environmental Science and Engineering, University of Science and Technology of China, Hefei 230026, China

ARTICLE INFO

Keywords:

Electrocatalytic hydrogenation
5-hydroxymethylfurfural
2
5-dihydroxymethylfuran
Buffer promotion
Co₃O₄

ABSTRACT

Electrocatalytic hydrogenation (ECH) represents a promising alternative to conventional hydrogenation techniques with high-pressure H₂ as a reductant. The proton-donating motif is an important factor governing the reaction efficiency but is usually overlooked in the ECH process. Herein, on the basis of density functional theory (DFT) predictions and experimental validations, we demonstrate that proton-buffer salts such as phosphate, carbonate and borate can greatly promote ECH efficiency. The DFT results predict that the buffer species can outperform water in donating protons for ^{*}C=O hydrogenation into ^{*}C-OH via the Langmuir-Hinshelwood or proton-coupled electron transfer (PCET) mechanism, thus promoting the hydrogenation of carbonyl compounds. The experimental results demonstrate that with the buffer-promoting effects, 5-hydroxymethylfurfural (HMF) can be effectively converted at an efficiency of 96 % into the value-added 2,5-dihydroxymethylfuran (DHMF) with a yield of 80 % over cobalt oxide (Co₃O₄) nanoarray catalysts under near-neutral buffer electrolyte. *In situ* Raman analysis and kinetic isotope experimental results reveal that the real mechanism is a combined Langmuir-Hinshelwood and PCET process. Such a buffer-promoting strategy also exhibits wide applicability in ECH of various other carbonyl compounds with different electrode catalysts. This work may provide a deep understanding of the ECH process and open up new opportunities to design effective systems for the conversion of HMF into value-added products.

1. Introduction

Hydrogenation is one of the most fundamental transformations in organic synthesis, spanning from fine chemical synthesis, pharmaceutical production, biomass valorization, etc. [1–4] Hydrogenation with H₂ as a hydrogen donor is the main commercialized hydrogenation method. However, harsh conditions, such as high temperature and H₂ pressure, remain a major challenge from the view of sustainability [5–8]. Moreover, the use of noble metal (e.g., Pd, Pt, Ru and Au)-based catalysts makes catalytic hydrogenation not economically friendly [2–4]. Electrocatalytic hydrogenation (ECH) should be an attractive alternative to conventional hydrogenation due to its various advantages, such as free of H₂ input, running at room temperature, a cleaner process and simpler to operate [9–12]. Moreover, the ECH would be increasingly

competitive in current society devoted to achieving carbon neutrality, as the cost of electricity generated from renewable sources such as wind, hydraulic power, and solar energy continues to decline [13,14]. As a consequence, the conversion of biomass into biofuels and value-added chemicals via ECH has attracted increasing attention [8,13,15–17]. 5-hydroxymethylfurfural (HMF), a six-carbon furanic carbonyl compound derived mainly from lignocellulosic biomass, has potential as an alternative commodity chemical to fossil-fuel-based platform chemicals [18,19]. Selective hydrogenation of the carbonyl is a critical step to upgrade HMF into many valued chemicals [7,20,21].

Understanding the mechanism of ECH is essential to designing a highly efficient catalytic system. In a typical C=O hydrogenation process, two hydrogen atoms are transferred. However, protons and electrons can be transferred from the same donor or different donors,

^{*} Corresponding authors.

E-mail addresses: liuwujun@mail.ustc.edu.cn (W.-J. Liu), hqyu@ustc.edu.cn (H.-Q. Yu).

¹ These authors contributed equally to this work.

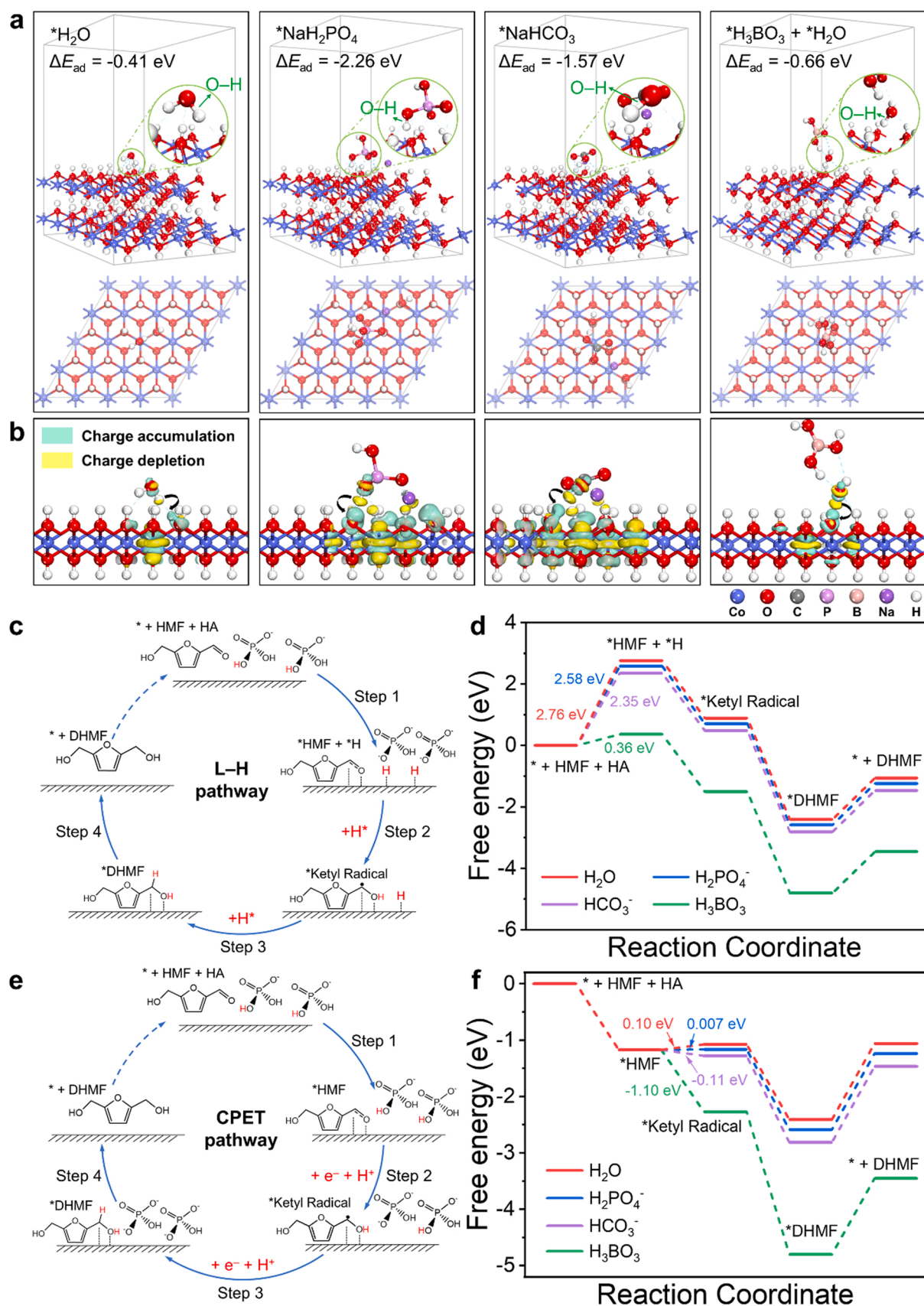


Fig. 1. DFT calculations of ECH with proton donors on the Co(OH)₂ surface. (a) Energy-minimized configurations of different proton donors (H₂O, NaH₂PO₄, NaHCO₃, and H₃BO₃ + H₂O) adsorption on the (001) surface of Co(OH)₂ and (b) corresponding charge density difference analysis. The ΔE_{ad} is the adsorption energy of the proton donors on Co(OH)₂. Isosurfaces are 0.03 eV/Å³. Electrochemical HMF reduction pathways: (c) L-H pathway and (d) free energy diagram. (e) CPET pathway and (f) the free energy diagram. The HA represents the proton donors. All the optimized configurations of intermediates are shown in Fig. S1.

simultaneously or separately. Based on the proton and electron sources, ECH can occur via two types of mechanisms. One is the Langmuir-Hinshelwood (L-H) mechanism, in which the proton first obtains an electron from the electrode to form an adsorbed hydrogen (H^*); then, the H^* reacts with the adsorbed $C=O$ to form $C-OH$ [22,23]. Another mechanism is proton-coupled electron transfer (PCET), in which protons and electrons are transferred to the reactant from different sources. According to the transfer sequence, the PCET mechanism can be further divided into 1) PT-ET, proton transfer followed by electron transfer; 2) ET-PT, electron transfer followed by proton transfer; and 3) concerted proton and electron transfer (CPET), in which protons and electrons are transferred simultaneously [23–25].

Previous studies have demonstrated that the proton and electron transfer is highly dependent on the catalyst structure, cathodic potential, and electrolyte pH [18,26–30]. However, the proton donor, an important factor influencing proton and electron transfer, seems to be overlooked. There are several potential proton donors in a typical aqueous electrolyte, i.e., H_2O , H_3O^+ , and some buffer species. However, in almost all previous studies, either H_2O or H_3O^+ is considered the proton source even in the presence of a buffer electrolyte [23,28,31–34]. Although the buffer-promoting effect has been reported in the hydrogen evolution reaction (HER), [24,35] its role in the ECH process remains

unknown.

In this work, with the DFT predictions and experimental validations, we demonstrate that proton-buffer salts such as phosphate, carbonate and borate could effectively promote the ECH efficiency by donating protons to the reactant. With the buffer-promoting effect, HMF was effectively converted into value-added 2,5-dihydroxymethylfuran (DHMF) over a Co_3O_4 nanoarray catalyst. We also found that the buffer-promoting effect had a wide applicability in the ECH of various other carbonyl compounds with different electrode catalysts.

2. Experimental methods

2.1. Preparation of the Co_3O_4 nanosheet array electrode

The Co_3O_4 nanosheet array was grown on a nickel foam using a hydrothermal approach [36]. In a typical procedure, $Co(NO_3)_2 \cdot 6H_2O$ (0.436 g, 1.5 mmol), NH_4F (0.111 g, 3 mmol) and urea (0.450 g, 7.5 mmol) were dissolved in 50 mL water and stirred to form a clear solution. Nickel foam (1 cm \times 2.5 cm) was cleaned with ethanol and 1 M H_2SO_4 to remove the surface organics and oxides. The aqueous solution and the Ni foam were transferred to a 100 mL Teflon-lined stainless-steel autoclave, which was sealed and maintained at 110 $^{\circ}C$ for 1.5 h. After

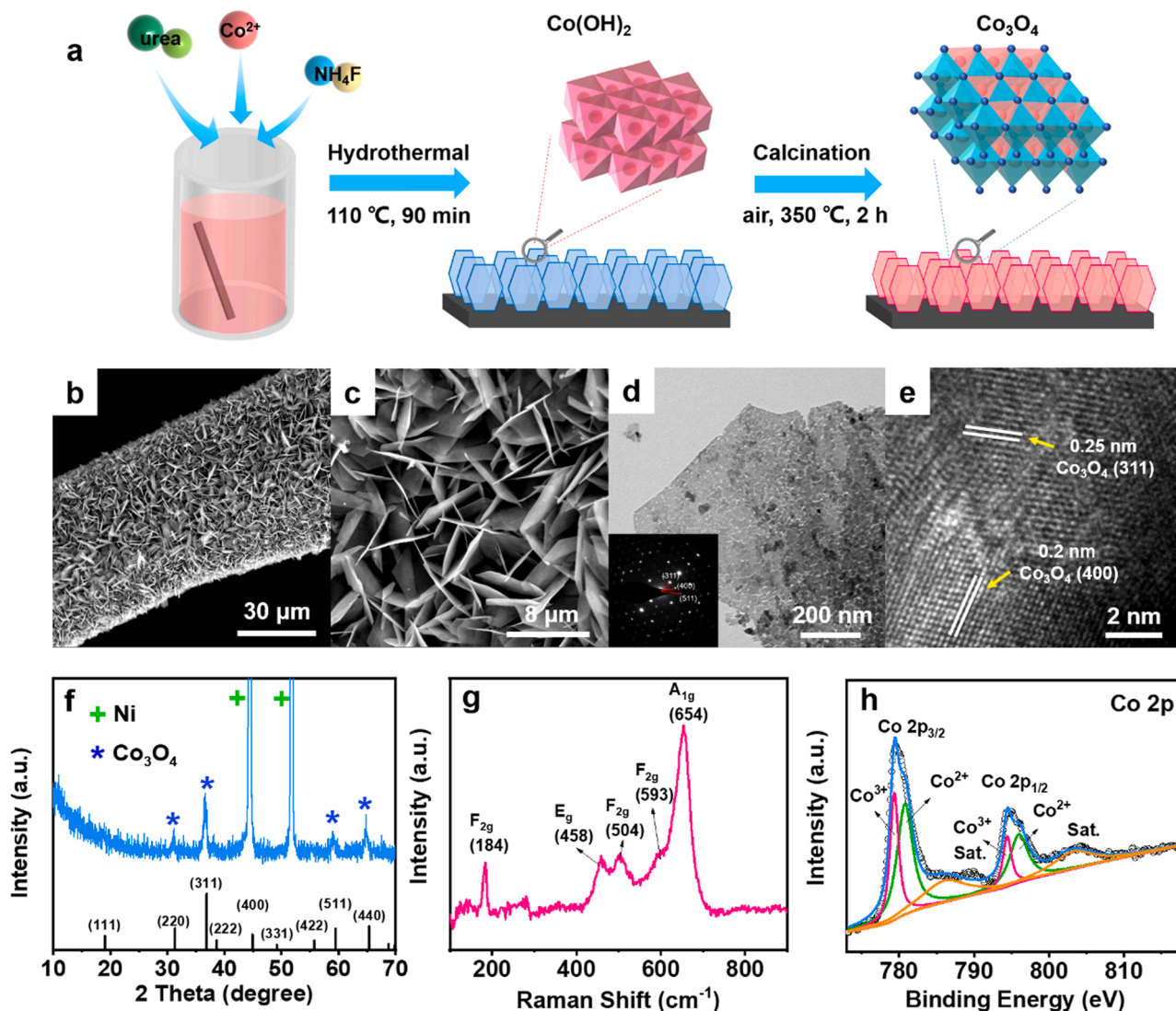


Fig. 2. Synthesis and characteristics of Co_3O_4 NSA. (a) Schematic synthesis of Co_3O_4 NSA. (b–c) SEM, (d) TEM, (e) HRTEM images, (f) X-ray diffraction pattern, (g) Raman spectrum, (h) XPS $Co\ 2p$ spectrum of the as-synthesized Co_3O_4 NSA.

cooling to room temperature, the nickel foam with pink film was rinsed several times with deionized water. Finally, the samples were annealed in air at 350 °C for 2 h in a muffle furnace. The composition and structure features were analysed with various methods presented in [Supplementary Materials](#) Text S2.

2.2. Electrochemical tests

All electrochemical experiments were conducted on an electrochemical workstation (CHI 750e, CH Instruments Co., China) at ambient temperature. Linear sweep voltammetry (LSV) and chronoamperometric experiments were conducted in a single-cell reactor with a three-electrode system, in which the glassy carbon electrode served as the working electrode, Ag/AgCl served as the reference electrode, and Pt wire served as the counter electrode. The LSV test was conducted at a scan rate of 50 mV/s. A total of 5.0 mg of active catalyst (Co₃O₄ NSA) was dispersed into anhydrous ethanol, with the addition of Nafion solution (50 μL), and then ultrasonication for 60 min to achieve a homogeneous ink. Then, 5 μL of the catalyst ink was pipetted onto the glassy carbon electrode to form a work electrode. The diameter of glassy carbon electrode was 3 mm and its surface area was calculated as 0.07 cm².

For the cathodic hydrogenation of HMF, an H-type cell with a three-electrode system was adopted, in which anode and cathode chambers were separated by a cation exchange membrane (CMI-7000, Membranes Inc., USA). Ag/AgCl was used as the reference electrode. The electrolyte volume was 18 mL in both chambers, and the size of the electrode immersed in the electrolyte was controlled to be 1 cm × 2 cm. For cathodic hydrogenation, the cathodic chamber was filled with 10 mM HMF in different electrolytes, while the anode chamber was filled with 0.1 M Na₂SO₄. For other powder catalysts, the working electrode was prepared by dropping 5 mg of catalyst ink onto carbon paper. For other substrates, the concentration of the reactants was 10 mM.

3. Results and discussion

3.1. Activation roles of buffer species on ECH by DFT calculations

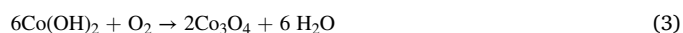
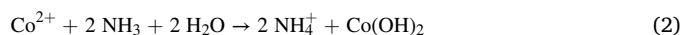
To explore the effect of buffer species on the electrocatalytic performance, DFT calculations were performed to reveal the configurations and electronic structures at the interface of the buffer species and catalyst surface. The adsorption configurations of the three common buffers (NaH₂PO₄, NaHCO₃, and H₃BO₃) on the (001) surface of Co(OH)₂ were investigated and compared with that of H₂O ([Fig. 1a](#)). Among them, H₃BO₃ coupled with H₂O molecules to donate protons through H₃BO₃ + H₂O → B(OH)₄[−] + H⁺. In comparison with H₂O (ΔE_{ad} = −0.41 eV), buffer species exhibited a more negative adsorption energy (ΔE_{ad} = −0.66~−2.26 eV), reflecting a stronger interaction with the Co(OH)₂ catalyst. Moreover, the charge density difference analysis also displays more significant charge transfer from the buffer proton donors to the Co(OH)₂ catalyst ([Fig. 1b](#)), which is consistent with the trends of the adsorption energy results. Furthermore, the O–H bond length of the different proton donors adsorbed on the (001) surface of Co(OH)₂ was longer than that of the free species ([Table S1](#)). These results imply that the O–H bonds of the species adsorbed on the Co(OH)₂ catalyst were weakened and favorable for dehydrogenation.[\[37\]](#) Among all the proton donors, the buffer anions exhibited a higher activity than that of the H₂O molecule with a longer O–H bond length of 1.008–1.042 Å and a higher elongation ratio of 3.07–6.98 % in contrast to the free molecules ([Table S1](#)).

To further examine the role of various proton donors in ECH, the thermodynamic properties of the HMF conversion reaction were calculated by involving the buffer species. Two distinct electron transfer pathways for the ECH of carbonyl compounds have been reported on the basis of the different intermediates on the catalyst surface, i.e., the L-H pathway and CPET pathway ([Fig. 1c](#) and [e](#)) [\[15,22,38\]](#). For the L-H pathway, the formation of adsorbed atomic hydrogen (H*) requires the

highest extra energy ([Fig. 1d](#) and [Table S2](#)). In contrast with the additional energy of Step 1 with the H₂O molecule (2.76 eV), the lower additional energy of ECH with buffer species as the proton donors (0.36–2.58 eV) is beneficial for the formation of *H. With respect to the CPET pathway, the Gibbs free energy change (ΔG) for the formation of *Ketyl radical (Step 2) from H₂O was higher than that from H₂PO₄[−], HCO₃[−], and H₃BO₃ + H₂O ([Fig. 1f](#) and [Table S3](#)). As a result, the *Ketyl radical prefers to be generated from the reaction with buffer species rather than H₂O molecules. These results indicate that the buffer species promote the generation of adsorbed hydrogen species in the L-H pathway and *Ketyl radical in the CPET pathway, which may contribute to the enhanced ECH efficiency of HMF to DHMF.

3.2. Synthesis and characteristics of the catalyst

To experimentally demonstrate the above DFT predictions, we constructed an ECH system over a Co₃O₄ nanosheet array electrode, in which Co₃O₄ can be reconstructed to Co(OH)₂ under negative potential. The Co₃O₄ NSA electrode was prepared via a facile two-step method described as follows ([Fig. 2a](#)): first, NH₃ could be continually produced from the slow hydrolysis of urea under hydrothermal conditions ([Eq. 1](#)). Then, the Co hydroxide (Co(OH)₂) nanosheets grow on the Ni foam via the reaction between Co(NO₃)₂ and NH₃ ([Eq. 2](#)). In this process, the controlled crystal growth under low supersaturation conditions created by the slow but continual release of NH₃ could facilitate the formation of ultrathin hydroxide nanosheets ([Fig. S2](#)). The as-synthesized Co(OH)₂ nanosheets were then annealed in air under a slow heating rate. The Co (II) species were partially oxidized into Co(III), while Co(OH)₂ was dehydrated and converted into Co₃O₄ ([Eq. 3](#)).



The morphology of the as-synthesized Co₃O₄ NSA was characterized with scanning electron microscopy (SEM) and transmission electron microscopy (TEM). The SEM images in [Fig. 2b](#) and [c](#) show that the as-synthesized electrode material consisted of thin nanosheets vertically aligned on the conducting Ni foam and fully covering the whole substrate, forming a three-dimensional nanoarray electrode. From the TEM image ([Fig. 2d](#)), some small particles in a single nanosheet were identified, and the nanosheet exhibited a polycrystalline structure. The high-resolution TEM (HRTEM) image ([Fig. 2e](#)) further confirms the presence of a polycrystal structure in the nanosheet, in which the lattice distances of 0.25 and 0.29 nm belonged to the (311) and (220) crystal planes of Co₃O₄, respectively [\[39,40\]](#). The XRD pattern of the as-synthesized electrode material is presented in [Fig. 2f](#). The peaks at 31.3°, 36.8°, 59.4°, and 65.2° matched the (220), (311), (511), and (440) planes of Co₃O₄ (JCPDS No. 76–1802), respectively. The XRD peaks located at 44.6° and 51.9° were assigned to the (111) and (200) planes of metallic Ni foam, respectively (JCPDS No. 70–0989). The Raman spectrum ([Fig. 2g](#)) displays five peaks at 184, 458, 504, 593, and 654 cm^{−1}, and these peaks could be attributed to the F_{2g}, E_g, F_{2g}, F_{2g}, and A_{1g} vibration modes of Co₃O₄, respectively [\[41,42\]](#). The surface chemistry of the Co₃O₄ NSA surface was analysed with XPS. In the survey spectrum ([Fig. S3a](#)), the peaks at approximately 530.1 and 795.43 eV were assigned to O 1s and Co 2p, respectively. In the high-resolution Co 2p spectrum ([Fig. 2h](#)), the peaks located at 779.3 and 794.4 eV were ascribed to the Co³⁺ species, and the peaks at 780.8 and 796.0 eV were assigned to the Co²⁺ species [\[39,43\]](#). In the O 1s spectrum ([Fig. S3b](#)), the peaks located at 529.7, 531.1, and 532.3 eV were attributed to lattice O from metal-oxygen bonds, adsorbed O from surface hydroxy or adsorbed oxygen species, and O from the surface of absorbed H₂O, respectively [\[44\]](#).

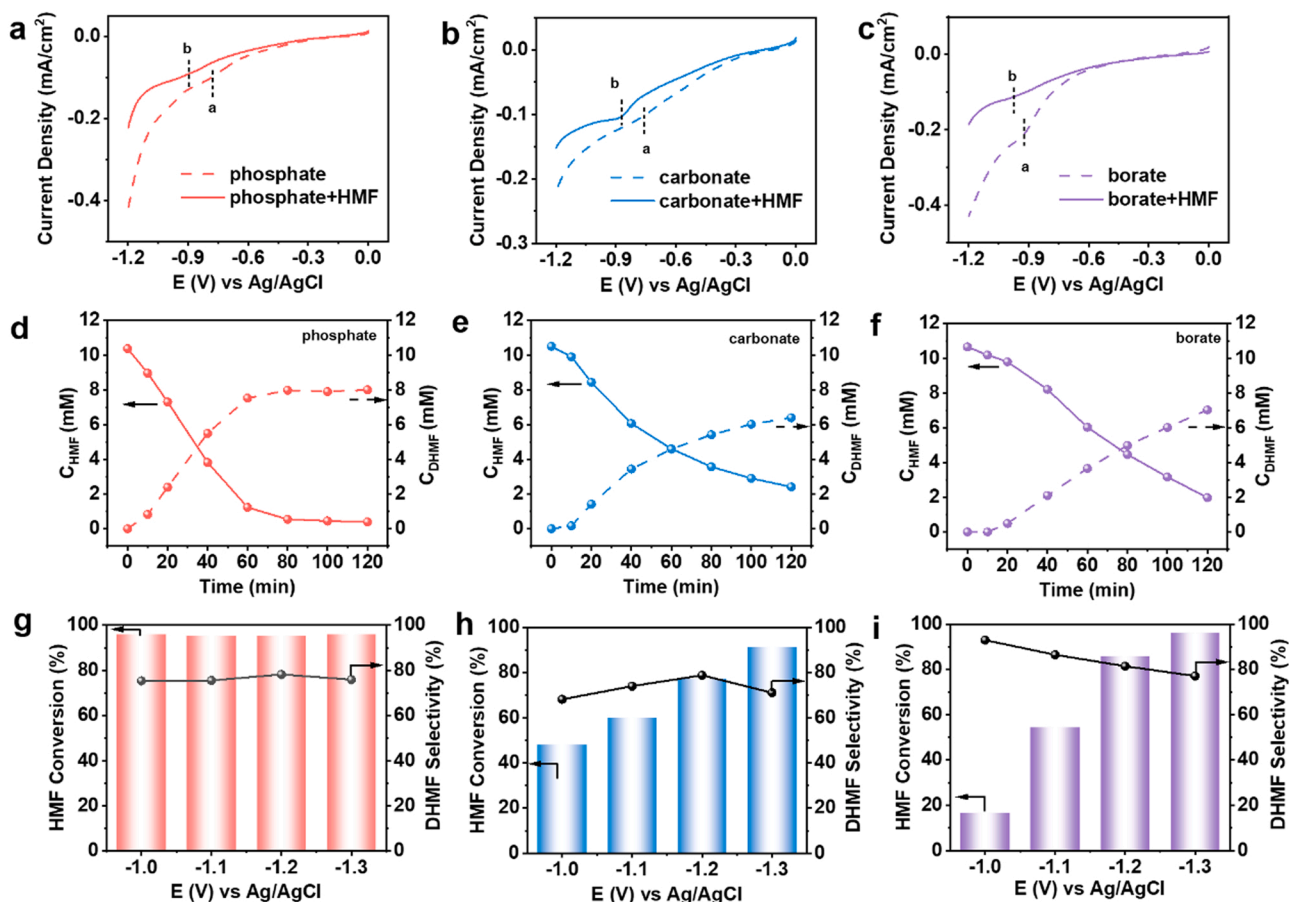


Fig. 3. LSV curves of Co₃O₄ NSA in 0.1 M buffer electrolytes with and without 10 mM HMF: (a) phosphate, (b) carbonate, and (c) borate. Concentration changes of HMF and DHMF in 0.1 M buffer electrolytes during the chronoamperometry test at -1.2 V vs Ag/AgCl: (d) phosphate, (e) carbonate, (f) borate. Conversion of HMF and selectivity of DHMF under different potentials in different buffer solutions: (g) phosphate, (h) carbonate, and (i) borate. Buffer concentration: 0.1 M (concentrations of conjugate acid and conjugate base in a 1:1 ratio), HMF concentration: 10 mM.

3.3. ECH of HMF

After the synthesis and structural analysis of the catalyst, its ECH performance toward HMF was experimentally evaluated to validate the DFT predictions. Three typical protic buffers, namely, phosphate (NaH₂PO₄/Na₂HPO₄), carbonate (NaHCO₃/Na₂CO₃), and borate (H₃BO₃/Na₂B₄O₇), were selected as buffer electrolytes for the ECH. In the blank phosphate buffer solution (Fig. 3a), a reduction peak (peak a) could be observed at -0.78 V, which could be ascribed to the reduction of Co₃O₄ due to the interaction of phosphate species with the catalyst surface [45,46]. After adding HMF, a new broad reduction peak (peak b) appeared at -0.9 V, which could be attributed to the adsorption or reduction of HMF [32,47]. Meanwhile, the addition of HMF greatly inhibited the HER current compared to the blank phosphate electrolyte, implying that the ECH process occurred under this condition. Similar results could also be found in the carbonate and borate buffers (Fig. 3b and c), in which the current density also decreased sharply when HMF was added. We emphasized that the main contribution was from conjugate acid by conducting linear sweep voltammetry (LSV) tests in each buffer component separately (Fig. S4). The LSV curves were collected in a nonbuffered Na₂SO₄ solution to investigate the influence of free protons on HMF hydrogenation. As shown in Fig. S5, Na₂SO₄ with the same pH showed a significantly low current with or without HMF, supporting the hypothesis that the buffer species can directly react on the electrode under proper potential.

After the LSV test, the ECH process was investigated with the chronoamperometric method at a constant potential of -1.2 V vs Ag/AgCl. As shown in Fig. 3d-f, the conversion ratios of HMF reached 96.0 %, 77.1 %, and 81.1 % with DHMF selectivities of 80.0 %, 79.0 % and 81.4 % in phosphate, carbonate and borate buffers, respectively.

The chronoamperometric test was also conducted under different potentials. It was obvious that hydrogenation occurred most easily in phosphate, with a stable HMF conversion at approximately 96.0 % and a steady selectivity at approximately 80 % from -1.0 to -1.3 V (Fig. 3g). For carbonate, HMF conversion grew progressively from 48.0 % to 92.0 %

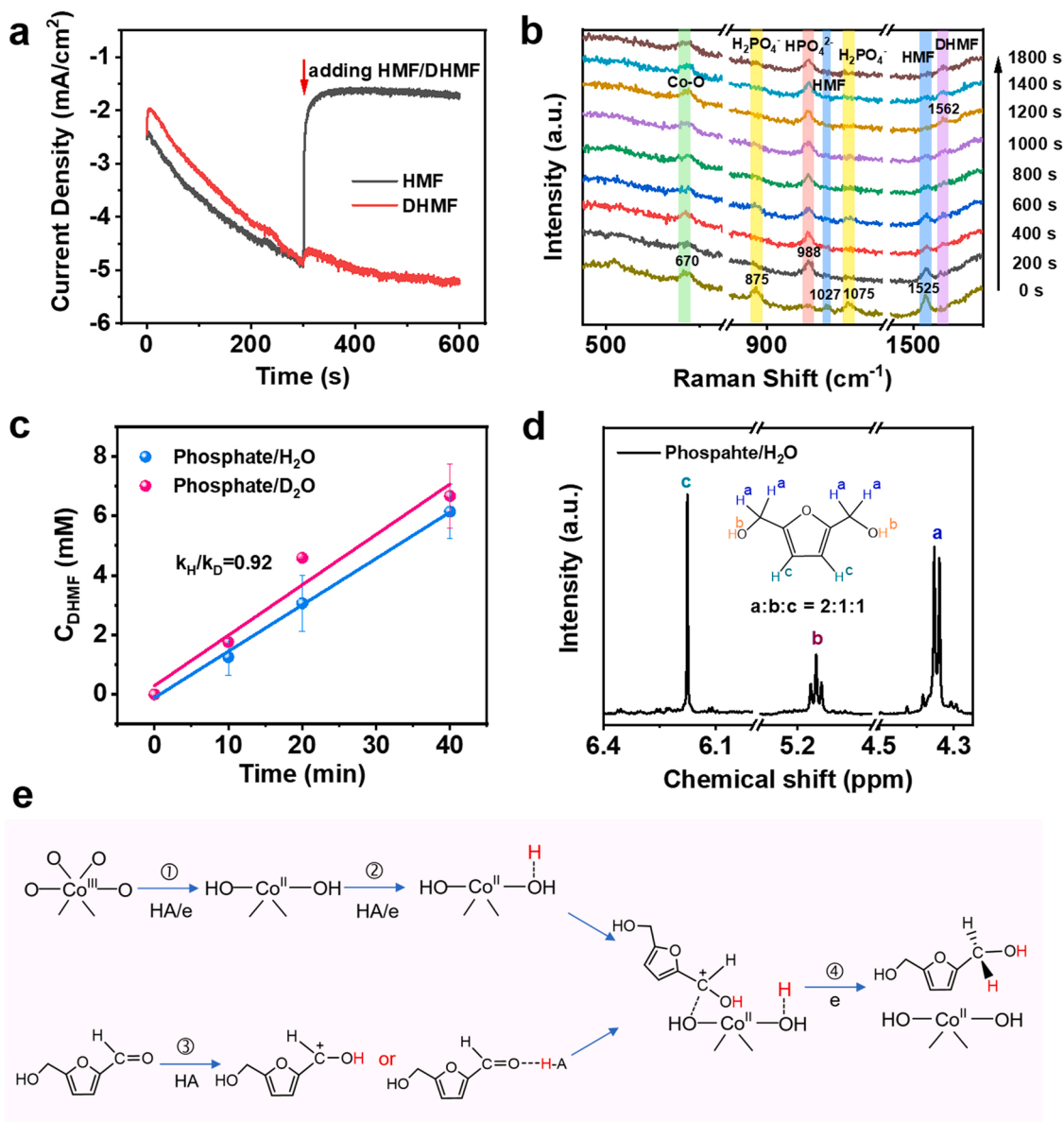


Fig. 4. (a) The current changes after adding 10 mM HMF or DHMF into blank phosphate solution during the chronoamperometry test. Potential: -1.2 V vs Ag/AgCl. (b) *In situ* Raman spectra during the chronoamperometry test in the NaH_2PO_4 electrolyte with HMF. Scan rate: 5 mV/s, constant potential: -1.2 V vs Ag/AgCl. (c) Kinetic isotope effect for ECH in phosphate electrolyte. (d) Nuclear magnetic resonance spectrum of ECH product of HMF obtained in phosphate/ H_2O . (e) The proposed reaction pathway in the real condition of the buffer-promoting ECH process.

%, and the selectivity peaked at 78.8 % and then decreased to 71.0 %, possibly due to the influence of the competitive HER process (Fig. 3h). For borate, the HMF conversion also increased with a negative potential, from 16.6 % at -1.0 V to 95.9 % at -1.3 V, but the selectivity experienced the reverse trend, decreasing from 92.9 % at -1.0 V to 77.0 % at -1.3 V (Fig. 3i). These results indicated that the HMF conversion and DHMF selectivity were closely related to the potential change. Phosphate had the highest conversion of HMF in the potential range, which was most likely due to the lowest pK_a value of H_2PO_4^- (7.2 for H_2PO_4^- , 10.2 for HCO_3^- , 9.2 for H_3BO_3), a signal of the facility to release the bonded hydrogen atom. This was also different from the prediction in the DFT calculations, in which H_3BO_3 had the lowest free energy in the selected pathways. It is assumed that the reaction rate was limited not only by the thermodynamic properties but also by the kinetic steps. In the ECH of HMF, the kinetic properties might be dominant, thus leading to the faster conversion of HMF in phosphate buffer than that in borate buffer. In addition, similar to the accelerated ECH process, the HER was

also boosted in the buffer electrolytes. As a result, the Faradaic efficiency (FE) for ECH of HMF was not high. It was calculated that the highest FE values for ECH were 26.3 %, 19.6 % and 20.9 % in the phosphate, carbonate, and borate buffers, respectively. (Fig. S10) Such low FE values indicate that ECH and HER might share the same H^* intermediate. Further investigations should be conducted to develop more efficient systems to suppress the HER side reaction.

3.4. ECH pathways and mechanism identification

The above results experimentally demonstrated the presence of buffer-promoting effects in the ECH of HMF into DHMF, and the DFT theoretically predicted two pathways in the buffer-promoting ECH, namely, the proton concerted electron transfer (PCET) pathway and Langmuir-Hinshelwood (L-H) pathway. However, the dominant pathway for the buffer-promoting ECH of HMF is still unknown. Herein, the pathway and mechanism for the buffer-promoting ECH of HMF were

experimentally identified.

First, it should be noted that in the DFT prediction, we constructed the DFT model over the $\text{Co}(\text{OH})_2$ catalyst but used Co_3O_4 as the experimental catalyst. The main reason for this selection is that under the negative potential of ECH, the high-valent metal oxide usually experiences a reductive reconstruction process to form lower-valent species. [48–50] In this work, we also observed a reductive reconstruction of Co_3O_4 into $\text{Co}(\text{OH})_2$, which was confirmed from the XRD and XPS results. The crystallinity of Co_3O_4 decreased sharply after the first 3 min, and no prominent peaks were identified from XRD (Fig. S11a). The chemical states of Co and O also changed, as observed in the XPS results. After 3 min of ECH, Co mainly existed in the $\text{Co}(\text{II})$ state (Fig. S11b), with O shifting from lattice oxygen to OH^- (Fig. S11c), implying the formation of $\text{Co}(\text{OH})_2$ in the ECH process. Such a reconstruction process was also verified based on the HRTEM image of the catalyst after the ECH reaction (Fig. S12). Furthermore, the reconstructed $\text{Co}(\text{OH})_2$ presented a better ECH activity for HMF, and it was thus adopted as the electrocatalyst for the ECH of HMF, rather than the non-calcined $\text{Co}(\text{OH})_2$ (Fig. S13).

A series of experiments were performed to identify which pathway dominated the buffer-promoting ECH of HMF. Fig. 4a displays the chronoamperometric profiles collected over the Co_3O_4 NSA catalyst with and without HMF. After adding HMF, the current showed an abrupt decrease, implying that the interactions between Co_3O_4 and buffer components were interfered by the surface-covered HMF. For comparison, the current remained well after the addition of DHMF. These results suggest that the aldehyde ($\text{HC}=\text{O}$) should be the exact group contributing to the adsorption of HMF onto the electrode, since the only difference between HMF and DHMF is the aldehyde group and hydroxyl group.

The in situ Raman spectra were collected to monitor the changes of different species on the electrode (Fig. 4b). The peaks located at 875 and 1075 cm^{-1} were attributed to H_2PO_4^- , and their intensities sharply decreased once a negative potential was applied. As a consequence, its proton abstraction product, HPO_4^{2-} , appeared at 988 cm^{-1} once the peak of H_2PO_4^- disappeared. This phenomenon implies that H_2PO_4^- could release protons rapidly to the electrode under a negative potential. The characteristic peak of HMF at 1525 cm^{-1} continued to decrease in the ECH process, accompanied by an increase in the peak located at 1562 cm^{-1} , which was attributed to the continuous formation of DHMF (Fig. S14). The sluggish generation of DHMF compared with the instant decrease in H_2PO_4^- suggests that the production of H^* was fast and the addition of H^* to HMF might be a rate-determining step. Under a negative potential, since the high-valence metal oxide usually experiences reductive reconstruction, the peak at 670 cm^{-1} in the reaction was mainly attributed to $\text{Co}(\text{OH})_2$ [41,51–53].

Cyclic voltammetry was used to examine the existence of H^* . First, the Pd/C was selected as a benchmark catalyst for generating H^* [54–56]. As shown in Fig. S15a, the oxidation peaks in the region of $0\sim -0.2\text{ V}$ (vs Ag/AgCl) could be attributed to adsorbed H (H_{abs}) and adsorbed H^* (H_{ads}) [54,55]. These results indicate that H^* could be formed both in Na_2SO_4 and phosphate buffer solution (PBS), but its production in PBS was greatly enhanced, suggesting that PBS could promote the generation of H^* . After dosing HMF, the peaks for both H_{abs} and H_{ads} disappeared quickly, implying that HMF might consume H^* (Fig. S15b). Similarly, when the electrocatalyst was changed from Pd/C to the as-used Co_3O_4 NSA/Ni foam catalyst, a broad H^* oxidation peak was found in the region of $0\sim -0.2\text{ V}$ (vs Ag/AgCl) [54] (Fig. S15c), and it could be quenched by the H^* scavenger tert-butanol (TBA). The current decreased after dosing HMF. These results demonstrate the existence and involvement of H^* in the ECH of HMF (Fig. S15d).

The kinetic isotope effect (KIE) was further adopted to explore the rate-determining step (RDS) in the buffer-promoting ECH process. Reactions with the different buffers were conducted in D_2O and compared with those in H_2O . It should be noted that the active hydrogen atoms on buffers and reactants were all deuterated in D_2O due to the fast D-H

exchange [57]. As shown in Fig. 4c, the reaction in phosphate followed zero-order kinetics, and $k_{\text{H}}/k_{\text{D}}$ was determined to be 0.92, suggesting that O-H cleavage was not the RDS and was independent of the reactant concentration [58]. For comparison, the ECH process in borate was also a zero-order reaction, but the $k_{\text{H}}/k_{\text{D}}$ was 2.1 (Fig. S16a), implying a primary KIE, [58] in which the cleavage of O-H was involved in the RDS. A second-order reaction and a $k_{\text{H}}/k_{\text{D}}$ of 1.4 were found for carbonate (Fig. S16b), indicating that the reaction rate in carbonate was dependent on the concentration of reactants in solution, and the normal secondary KIE suggests that a change in bond hybridization or a bond weakness was involved in RDS rather than bond cleavage [57].

The ECH products of HMF in phosphate/ H_2O and phosphate/ D_2O were separated and analysed with nuclear magnetic resonance (NMR) measurements. The product spectra in phosphate/ H_2O (Fig. 4d) gave exact signals of DHMF. The rapid exchange of H-D on the -OH of DHMF was evidenced by the NMR spectra. As shown in Fig. S17a, after adding several D_2O drops into $\text{DMSO}-d_6$, the peaks of hydrogen atoms on -OH disappeared rapidly, implying the occurrence of deuteration. Meanwhile, the product spectra obtained in phosphate/ D_2O show that three hydrogen atoms were deuterated (Fig. S17b), among which one atom on -OH was deuterated by the solvent D_2O and the other two were deuterated in the process of ECH by NaD_2PO_4 .

With the above results, we propose that the buffer-promoting ECH of HMF may follow a combination of L-H and PCET mechanisms (Fig. 4e). Generally, Co_3O_4 was reduced to $\text{Co}(\text{OH})_2$ under a negative potential (Step 1 in Fig. 4e). Then, H^* was formed on the electrode surface via the discharge of buffer components or their complexes with water (Step 2 in Fig. 4e). This process was accompanied by H_2 evolution, as observed in the experiments. The formation of H^* includes O-H cleavage; thus, a primary KIE can be observed if the H^* formation is the RDS. Meanwhile, due to the electrostatic interaction between the negatively charged carbonyl oxygen atom and hydrogen in proton donors, protonation of HMF would occur or at least a strong donor-acceptor complex could be formed (Step 3 in Fig. 4e) [59,60]. The electron on the electrode then served as a nucleophile to attack the positively charged carbon atom, and subsequently, H^* was added to complete the hydrogenation process (Step 4 in Fig. 4e). Due to the different proton-release abilities, the rate determining steps in phosphate, borate, and carbonate were Step 4, Step 2, and Step 3, respectively (Fig. 4e).

In details, for the phosphate buffer, the formation of H^* and protonation of HMF quickly occurred due to the small pKa value of H_2PO_4^- , leaving the second hydrogen addition (Step 4) as the RDS. Since H^* was a hydrogen atom adsorbed on the catalyst, the addition of H^* onto the Ketyl radical did not involve the cleavage of O-H, thus showing a secondary KIE [61]. Thus, the surface process governed its zero reaction order [62]. For borate, Step 2 could be the slowest step, as the pKa value of H_3BO_3 was higher than that of H_2PO_4^- , and an interaction between the buffer and catalyst was needed. Considering that H_3BO_3 combines with H_2O to donate protons, a primary KIE would appear when Step 2 was the RDS [61]. For carbonate, owing to the largest pKa of HCO_3^- , it was difficult for it to form a complex with HMF, leading to a low concentration of the complex and making Step 3 the RDS. In this process, the O-H in HCO_3^- was not cleaved but only weakened, matching the normal secondary KIE [58]. This process took place in the bulk solution so that the rate was dependent on the concentrations of HMF and HCO_3^- , leading to a second reaction order. Overall, the proposed mechanism can explain the experimental observation. To conclude, the buffer electrolyte could participate in the ECH reaction by promoting H^* generation and carbonyl activation, which was the main reason for the better performance in the buffer electrolyte than in the non-buffered electrolyte.

3.5. Generality of the buffer-promoting effect

After identification of the exact pathway for the buffer-promoting ECH of HMF to DHMF over the Co_3O_4 NSA catalyst, one would wonder whether such a buffer-promoting effect is also valid for other

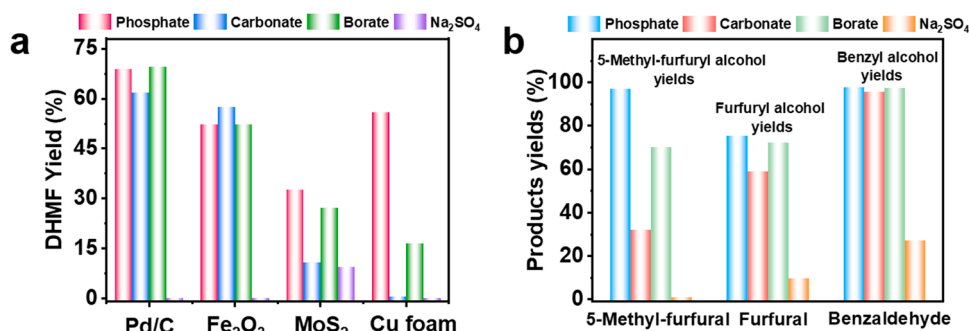


Fig. 5. (a) Electrohydrogenation of HMF on different electrocatalysts in different buffer electrolytes. (b) Electrohydrogenation of different aldehyde-containing substrates on Co₃O₄ NSA in different buffer electrolytes. Potential: -1.2 V vs Ag/AgCl, buffer concentration: 0.1 M (concentrations of conjugate acid and conjugate base in a 1:1 ratio), substrate concentration: 10 mM.

catalysts or substrates besides the Co₃O₄ NSA or HMF. To examine the generality of the buffer-promoting effect, the ECH of HMF was tested over different electrocatalysts in several buffer electrolytes. As the results showed, the buffer-promoting effect also existed over other electrocatalysts, especially the Pd/C and Fe₂O₃ catalysts (Fig. 5a). The ECH efficiencies in different buffers significantly outperformed those in a nonbuffered Na₂SO₄ solution. These results suggest the widespread existence of the buffer-promoting effects. Fig. 5b displays the ECH of three other aldehydes (e.g., 5-methylfurfural, furfural and benzaldehyde), showing that all these compounds presented higher hydrogenation efficiencies in the buffers than in the nonbuffered electrolyte. The yield of 5-methylfurfuryl alcohol in phosphate buffer reached 96.9 %, and the yields of benzyl alcohol reached 97.6 %, 95.5 %, and 97.1 % in phosphate, carbonate and borate, respectively, indicating that the buffer electrolytes greatly improved the ECH performance.

4. Conclusions

In this work, by combining DFT predictions and experimental investigations, we have demonstrated that proton-buffer salts such as phosphate, carbonate and borate can effectively promote the ECH of HMF over Co₃O₄ NSA electrocatalysts. With buffer-promoting effects, HMF could be efficiently converted into DHMF with high yields and selectivities. A combined proton concerted electron transfer (PCET) and Langmuir-Hinshelwood (L-H) pathway was identified as the main mechanism of the buffer-promoted ECH of HMF into DHMF. Such a buffer-promoting effect was also demonstrated to be effective with other electrocatalysts and substrates in addition to the Co₃O₄ NSA or HMF. We expect this work to provide a deep understanding of the ECH reaction and open up new opportunities to design effective systems for biomass conversion.

CRediT authorship contribution statement

Xiao-Qiang Pan: Data curation, Writing – original draft. **Xin-Yu Zhang:** DFT calculations. **Gui-Xiang Huang:** Writing – review & editing. **Shu-Chuan Mei:** Data curation. **Jia-Wei Huang:** Data curation. **Jie-Jie Chen:** Writing – review & editing. **Wu-Jun Liu:** Writing – original draft, Writing – review & editing, Funding acquisition. **Han-Qing Yu:** Writing – review & editing, Funding acquisition.

Declaration of Competing Interest

The authors declare that they have no known competing financial interests or personal relationships that could have appeared to influence the work reported in this paper.

Data Availability

Data will be made available on request.

Acknowledgments

The authors gratefully acknowledge the support from the National Key Technical Research and Development Program of China (2020YFD1100402-2), the National Natural Science Foundation of China (22122608, 21976170, U20A20325 and 51821006), and the Fundamental Research Funds for the Central Universities (WK3530000009, YD2400002001).

Appendix A. Supporting information

Supplementary data associated with this article can be found in the online version at doi:10.1016/j.apcatb.2022.122191.

References

- [1] D. Wang, D. Astruc, The golden age of transfer hydrogenation, *Chem. Rev.* 115 (2015) 6621–6686.
- [2] K. Liu, R. Qin, N. Zheng, Insights into the interfacial effects in heterogeneous metal nanocatalysts toward selective hydrogenation, *J. Am. Chem. Soc.* 143 (2021) 4483–4499.
- [3] X. Lan, T. Wang, Highly selective catalysts for the hydrogenation of unsaturated aldehydes: a review, *ACS Catal.* 10 (2020) 2764–2790.
- [4] M. Luneau, J.S. Lim, D.A. Patel, E.C.H. Sykes, C.M. Friend, P. Sautet, Guidelines to achieving high selectivity for the hydrogenation of α,β -unsaturated aldehydes with bimetallic and dilute alloy catalysts: a review, *Chem. Rev.* 120 (2020) 12834–12872.
- [5] K.J. Carroll, T. Burger, L. Langenegger, S. Chavez, S.T. Hunt, Y. Roman-Leshkov, F. R. Brushett, Electrocatalytic hydrogenation of oxygenates using earth-abundant transition-metal nanoparticles under mild conditions, *ChemSusChem* 9 (2016) 1904–1910.
- [6] J. Carneiro, E. Nikolla, Electrochemical conversion of biomass-based oxygenated compounds, *Annu. Rev. Chem. Biomol. Eng.* 10 (2019) 85–104.
- [7] C.H. Lam, W. Deng, L. Lang, X. Jin, X. Hu, Y. Wang, Minireview on bio-oil upgrading via electrocatalytic hydrogenation: connecting biofuel production with renewable power, *Energy Fuels* 34 (2020) 7915–7928.
- [8] G. Chen, L. Liang, N. Li, X. Lu, B. Yan, Z. Cheng, Upgrading of bio-oil model compounds and bio-crude into biofuel by electrocatalysis: a review, *ChemSusChem* 14 (2021) 1037–1052.
- [9] Q. Liu, Y. Lin, S. Gu, Z. Cheng, L. Xie, S. Sun, L. Zhang, Y. Luo, A.A. Alshehri, M. S. Hamdy, Q. Kong, J. Wang, X. Sun, Enhanced n2-to-nh3 conversion efficiency on cu3p nanoribbon electrocatalyst, *Nano Res.* 15 (2022) 7134–7138.
- [10] J. Liang, Q. Liu, A.A. Alshehri, X. Sun, Recent advances in nanostructured heterogeneous catalysts for n-cycle electrocatalysis, *Nano Res. Energy* 1 (2022).
- [11] H.-j. Chen, Z.-q. Xu, S. Sun, Y. Luo, Q. Liu, M.S. Hamdy, Z.-s. Feng, X. Sun, Y. Wang, Plasma-etched ti2o3 with oxygen vacancies for enhanced nh3 electrosynthesis and zn-n2 batteries, *Inorg. Chem. Front.* 9 (2022) 4608–4613.
- [12] Q. Liu, G. Wen, D. Zhao, L. Xie, S. Sun, L. Zhang, Y. Luo, A. Ali Alshehri, M. S. Hamdy, Q. Kong, X. Sun, Nitrite reduction over Ag nanoarray electrocatalyst for ammonia synthesis, *J. Colloid Interface Sci.* 623 (2022) 513–519.
- [13] S.A. Akhade, N. Singh, O.Y. Gutier, Y. Liu, A. Karkamkar, R.S. Weber, A. B. Padmaperuma, M.-S. Lee, G.A. Whyatt, M. Elliott, J.E. Holladay, J.L. Male, J. A. Lercher, R. Rousseau, V.-A. Glezakou, Electrocatalytic hydrogenation of biomass-derived organics: a review, *Chem. Rev.* 120 (2020) 11370–11419.

- [14] Y.P. Wijaya, K.J. Smith, C.S. Kim, E.L. Gyenge, Electrocatalytic hydrogenation and depolymerization pathways for lignin valorization: toward mild synthesis of chemicals and fuels from biomass, *Green. Chem.* 22 (2020) 7233–7264.
- [15] K. Li, Y. Sun, Electrocatalytic upgrading of biomass-derived intermediate compounds to value-added products, *Chem. Eur. J.* 24 (2018) 18258–18270.
- [16] F.W.S. Lucas, R.G. Grim, S.A. Tacey, C.A. Downes, J. Hasse, A.M. Roman, C. A. Farberow, J.A. Schaidle, A. Holewinski, Electrochemical routes for the valorization of biomass-derived feedstocks: from chemistry to application, *ACS Energy Lett.* (2021) 1205–1270.
- [17] Y. Kwon, K.J.P. Schouten, J.C. van der Waal, E. de Jong, M.T.M. Koper, Electrocatalytic conversion of furanic compounds, *ACS Catal.* 6 (2016) 6704–6717.
- [18] J.A. Lopez-Ruiz, U. Sanyal, J. Egbert, O.Y. Gutiérrez, J. Holladay, Kinetic investigation of the sustainable electrocatalytic hydrogenation of benzaldehyde on Pd/C: effect of electrolyte composition and half-cell potentials, *ACS Sustain. Chem. Eng.* 6 (2018) 16073–16085.
- [19] L. Hu, J. Xu, S. Zhou, A. He, X. Tang, L. Lin, J. Xu, Y. Zhao, Catalytic advances in the production and application of biomass-derived 2,5-dihydroxymethylfuran, *ACS Catal.* 8 (2018) 2959–2980.
- [20] Y. Nakagawa, M. Tamura, K. Tomishige, Catalytic reduction of biomass-derived furanic compounds with hydrogen, *ACS Catal.* 3 (2013) 2655–2668.
- [21] J. Zhu, G. Yin, Catalytic transformation of the furfural platform into bifunctionalized monomers for polymer synthesis, *ACS Catal.* 11 (2021) 10058–10083.
- [22] C.J. Bondue, M.T.M. Koper, A mechanistic investigation on the electrocatalytic reduction of aliphatic ketones at platinum, *J. Catal.* 369 (2019) 302–311.
- [23] K. Koh, U. Sanyal, M.-S. Lee, G. Cheng, M. Song, V.-A. Glezakou, Y. Liu, D. Li, R. Rousseau, O.Y. Gutiérrez, A. Karkamkar, M. Derewinski, J.A. Lercher, Electrochemically tunable proton-coupled electron transfer in Pd-catalyzed benzaldehyde hydrogenation, *Angew. Chem. Int. Ed.* 59 (2020) 1501–1505.
- [24] M.N. Jackson, O. Jung, H.C. Lamotte, Y. Surendranath, Donor-dependent promotion of interfacial proton-coupled electron transfer in aqueous electrocatalysis, *ACS Catal.* 9 (2019) 3737–3743.
- [25] D.C. Cantu, A.B. Padmaperuma, M.-T. Nguyen, S.A. Akhade, Y. Yoon, Y.-G. Wang, M.-S. Lee, V.-A. Glezakou, R. Rousseau, M.A. Lilga, A combined experimental and theoretical study on the activity and selectivity of the electrocatalytic hydrogenation of aldehydes, *ACS Catal.* 8 (2018) 7645–7658.
- [26] P. Zhou, Y. Chen, P. Luan, X. Zhang, Z. Yuan, S.-X. Guo, Q. Gu, B. Johannessen, M. Mollah, A.L. Chaffee, D.R. Turner, J. Zhang, Selective electrochemical hydrogenation of furfural to 2-methylfuran over a single atom Cu catalyst under mild pH conditions, *Green. Chem.* 23 (2021) 3028–3038.
- [27] C.J. Bondue, F. Calle-Vallejo, M.C. Figueiredo, M.T.M. Koper, Structural principles to steer the selectivity of the electrocatalytic reduction of aliphatic ketones on platinum, *Nat. Catal.* 2 (2019) 243–250.
- [28] P. Zhou, L. Li, V.S.S. Mosali, Y. Chen, P. Luan, Q. Gu, D.R. Turner, L. Huang, J. Zhang, Electrochemical hydrogenation of furfural in aqueous acetic acid media with enhanced 2-methylfuran selectivity using cupd bimetallic catalysts, *Angew. Chem. Int. Ed.* 61 (2022) e202117809.
- [29] X. Wang, Y. Jiao, L. Li, Y. Zheng, S.-Z. Qiao, Local environment determined reactant adsorption configuration for enhanced electrocatalytic acetone hydrogenation to propane, *Angew. Chem. Int. Ed.* 61 (2022) e202114253.
- [30] W. Xu, C. Yu, J. Chen, Z. Liu, Electrochemical hydrogenation of biomass-based furfural in aqueous media by Cu catalyst supported on N-doped hierarchically porous carbon, *Appl. Catal. B* 305 (2022), 121062.
- [31] X.H. Chadderdon, D.J. Chadderdon, T. Pfennig, B.H. Shanks, W. Li, Paired electrocatalytic hydrogenation and oxidation of 5-(hydroxymethyl)furfural for efficient production of biomass-derived monomers, *Green. Chem.* 21 (2019) 6210–6219.
- [32] J.J. Roynance, T.W. Kim, K.S. Choi, Efficient and selective electrochemical and photoelectrochemical reduction of 5-hydroxymethylfurfural to 2,5-bis(hydroxymethyl)furan using water as the hydrogen source, *ACS Catal.* 6 (2016) 1840–1847.
- [33] L. Liu, H. Liu, W. Huang, Y. He, W. Zhang, C. Wang, H. Lin, Mechanism and kinetics of the electrocatalytic hydrogenation of furfural to furfuryl alcohol, *J. Electroanal. Chem.* 804 (2017) 248–253.
- [34] J. Tan, W. Zhang, Y. Shu, H. Lu, Y. Tang, Q. Gao, Interlayer engineering of molybdenum disulfide toward efficient electrocatalytic hydrogenation, *Sci. Bull.* 66 (2021) 1003–1012.
- [35] K.E. Clary, M. Karayilan, K.C. McCleary-Petersen, H.A. Petersen, R.S. Glass, J. Pyun, D.L. Lichtenberger, Increasing the rate of the hydrogen evolution reaction in neutral water with protic buffer electrolytes, *Proc. Natl. Acad. Sci.* 117 (2020) 32947–32953.
- [36] Q. Yang, Z. Lu, Z. Chang, W. Zhu, J. Sun, J. Liu, X. Sun, X. Duan, Hierarchical Co₃O₄ nanosheet@nanowire arrays with enhanced pseudocapacitive performance, *RSC Adv.* 2 (2012) 1663–1668.
- [37] F. Sun, J. Qin, Z. Wang, M. Yu, X. Wu, X. Sun, J. Qiu, Energy-saving hydrogen production by chlorine-free hybrid seawater splitting coupling hydrazine degradation, *Nat. Commun.* 12 (2021) 4182.
- [38] A.J.F. Bard, L. R. Electrochemical Methods Fundamentals and Applications, second ed., Wiley, 2001.
- [39] J. Li, Z. Li, F. Ning, L. Zhou, R. Zhang, M. Shao, M. Wei, Ultrathin mesoporous Co₃O₄ nanosheet arrays for high-performance lithium-ion batteries, *ACS Omega* 3 (2018) 1675–1683.
- [40] X. Zhou, Z. Liu, Y. Wang, Y. Ding, Facet effect of Co₃O₄ nanocrystals on visible-light driven water oxidation, *Appl. Catal. B* 237 (2018) 74–84.
- [41] V.G. Hadjiev, M.N. Iliev, I.V. Vergilov, The Raman spectra of Co₃O₄, *J. Phys. Chem. C: Solid State Phys.* 21 (1988) L199–L201.
- [42] Y. Dou, Y. Wang, D. Tian, J. Xu, Z. Zhang, Q. Liu, B. Ruan, J. Ma, Z. Sun, S.X. Dou, Atomically thin Co₃O₄ nanosheet-coated stainless steel mesh with enhanced capacitive Na⁺ storage for high-performance sodium-ion batteries, *2D Mater.* 4 (2016), 015022.
- [43] Y. Zou, I.A. Kinloch, R.A. Dryfe, Mesoporous vertical Co₃O₄ nanosheet arrays on nitrogen-doped graphene foam with enhanced charge-storage performance, *ACS Appl. Mater. Interfaces* 7 (2015) 22831–22838.
- [44] Z. Wang, H. Liu, R. Ge, X. Ren, J. Ren, D. Yang, L. Zhang, X. Sun, Phosphorus-doped Co₃O₄ nanowire array: A highly efficient bifunctional electrocatalyst for overall water splitting, *ACS Catal.* 8 (2018) 2236–2241.
- [45] C.A. Gervasi, S.R. Biaggio, J.R. Vilche, A.J. Arvia, A kinetic study of the electroreduction of anodically formed cobalt oxide layers, *Electrochim. Acta* 36 (1991) 2147–2152.
- [46] C.A. Gervasi, Models of the electroreduction of passive layers on cobalt, *J. Braz. Chem. Soc.* 8 (1997) 169–173.
- [47] C.J. Bondue, M.T.M. Koper, Electrochemical reduction of the carbonyl functional group: The importance of adsorption geometry, molecular structure, and electrode surface structure, *J. Am. Chem. Soc.* 141 (2019) 12071–12078.
- [48] D. Ren, Y.L. Deng, A.D. Handoko, C.S. Chen, S. Malkhandi, B.S. Yeo, Selective electrochemical reduction of carbon dioxide to ethylene and ethanol on copper(I) oxide catalysts, *ACS Catal.* 5 (2015) 2814–2821.
- [49] W. Luo, Q. Zhang, J. Zhang, E. Moio, K. Zhao, A. Züttel, Electrochemical reconstruction of ZnO for selective reduction of CO₂ to CO, *Appl. Catal. B* 273 (2020), 119060.
- [50] J. Fu, F. Yao, T. Xie, Y. Zhong, Z. Tao, S. Chen, L. He, Z. Pi, K. Hou, D. Wang, X. Li, Q. Yang, In-situ growth of needle-like Co₃O₄ on cobalt foam as a self-supported cathode for electrochemical reduction of nitrate, *Sep. Purif. Technol.* 276 (2021), 119329.
- [51] A.V. Ravindra, B.C. Behera, P. Padhan, Laser induced structural phase transformation of cobalt oxides nanostructures, *J. Nanosci. Nanotechnol.* 14 (2014) 5591–5595.
- [52] M. Abu Sayeed, T. Herd, A.P. O'Mullane, Direct electrochemical formation of nanostructured amorphous Co(OH)₂ on gold electrodes with enhanced activity for the oxygen evolution reaction, *J. Mater. Chem. A* 4 (2016) 991–999.
- [53] U.M. Patil, R.V. Ghorpade, M.S. Nam, A.C. Nalawade, S. Lee, H. Han, S.C. Jun, Polyhipe derived freestanding 3D carbon foam for cobalt hydroxide nanorods based high performance supercapacitor, *Sci. Rep.* 6 (2016) 35490.
- [54] R. Liu, H. Zhao, X. Zhao, Z. He, Y. Lai, W. Shan, D. Bekana, G. Li, J. Liu, Defect sites in ultrathin Pd nanowires facilitate the highly efficient electrochemical hydrodechlorination of pollutants by H⁺ ads., *Environ. Sci. Technol.* 52 (2018) 9992–10002.
- [55] G. Jiang, M. Lan, Z. Zhang, X. Lv, Z. Lou, X. Xu, F. Dong, S. Zhang, Identification of active hydrogen species on palladium nanoparticles for an enhanced electrocatalytic hydrodechlorination of 2,4-dichlorophenol in water, *Environ. Sci. Technol.* 51 (2017) 7599–7605.
- [56] A. Zalinaeva, S. Baranton, C. Coutanceau, G. Jerkiewicz, Octahedral palladium nanoparticles as excellent hosts for electrochemically adsorbed and absorbed hydrogen, *Sci. Adv.* 3 (2017), e1600542.
- [57] M. Gomez-Gallego, M.A. Sierra, Kinetic isotope effects in the study of organometallic reaction mechanisms, *Chem. Rev.* 111 (2011) 4857–4963.
- [58] Y. Lin, C. Deng, L. Wu, Y. Zhang, C. Chen, W. Ma, J. Zhao, Quantitative isotope measurements in heterogeneous photocatalysis and electrocatalysis, *Energy Environ. Sci.* 13 (2020) 2602–2617.
- [59] G.A. Olah, D.H. O'Brien, Stable carbonium ions. Xlii. La protonated aliphatic aldehydes, *J. Am. Chem. Soc.* 89 (1967) 3582–3586.
- [60] P.S. The Chemistry of the Carbonyl Group, John Wiley & Sons Ltd, New York, 1966.
- [61] W. Ma, S. Xie, T. Liu, Q. Fan, J. Ye, F. Sun, Z. Jiang, Q. Zhang, J. Cheng, Y. Wang, Electrocatalytic reduction of CO₂ to ethylene and ethanol through hydrogen-assisted C–C coupling over fluorine-modified copper, *Nat. Catal.* 3 (2020) 478–487.
- [62] P. Liu, Y. Zhao, R. Qin, S. Mo, G. Chen, L. Gu, D.M. Chevrier, P. Zhang, Q. Guo, D. Zang, B. Wu, G. Fu, N. Zheng, Photochemical route for synthesizing atomically dispersed palladium catalysts, *Science* 352 (2016) 797–800.